



## Variability of X-ray binaries from an oscillating hot corona

C. Cabanac, G. Henri, P.-O. Petrucci, J. Malzac, Jorge Ferreira, T. M. Belloni

### ► To cite this version:

C. Cabanac, G. Henri, P.-O. Petrucci, J. Malzac, Jorge Ferreira, et al.. Variability of X-ray binaries from an oscillating hot corona. Monthly Notices of the Royal Astronomical Society, 2010, 404, pp.738-748. 10.1111/j.1365-2966.2010.16340.x . hal-00631839

**HAL Id: hal-00631839**

**<https://hal.science/hal-00631839>**

Submitted on 30 Nov 2021

**HAL** is a multi-disciplinary open access archive for the deposit and dissemination of scientific research documents, whether they are published or not. The documents may come from teaching and research institutions in France or abroad, or from public or private research centers.

L'archive ouverte pluridisciplinaire **HAL**, est destinée au dépôt et à la diffusion de documents scientifiques de niveau recherche, publiés ou non, émanant des établissements d'enseignement et de recherche français ou étrangers, des laboratoires publics ou privés.



Distributed under a Creative Commons Attribution 4.0 International License

# Variability of X-ray binaries from an oscillating hot corona

C. Cabanac,<sup>1,2,3\*</sup> G. Henri,<sup>3</sup> P.-O. Petrucci,<sup>3</sup> J. Malzac,<sup>1</sup> J. Ferreira<sup>3</sup>  
and T. M. Belloni<sup>4</sup>

<sup>1</sup>Centre d'Étude Spatiale des Rayonnements, CNRS-UPS, 9 Avenue du Colonel Roche, 31028 Toulouse Cedex 4, France

<sup>2</sup>School of Physics and Astronomy, University of Southampton, Southampton SO17 1BJ

<sup>3</sup>Laboratoire d'Astrophysique de Grenoble–Université Joseph-Fourier/CNRS UMR 5571, BP 53, F-38041 Grenoble, France

<sup>4</sup>INAF-Osservatorio Astronomico di Brera, Via E. Bianchi 46, I-23807 Merate (LC), Italy

Accepted 2010 January 12. Received 2010 January 12; in original form 2009 September 9

## ABSTRACT

The spectral and timing properties of an oscillating hot thermal corona are investigated. This oscillation is assumed to be due to a magneto-acoustic wave propagating within the corona and triggered by an external, non-specified, excitation. A cylindrical geometry is adopted and, neglecting the rotation, the wave equation is solved for different boundary conditions. The resulting X-ray luminosity, through thermal Comptonization of embedded soft photons, is then computed analytically, assuming linear dependence between the local pressure disturbance and the radiative modulation. These calculations are also compared to Monte Carlo simulations. The main results of this study are as follows. (1) The corona plays the role of a low bandpass medium, its response to a white noise excitation being a flat-top noise power spectral density (PSD) at low frequencies and a red noise at high frequency. (2) Resonant peaks are present in the PSD. Their powers depend on the boundary conditions chosen and, more specifically, on the impedance adaptation with the external medium at the corona inner boundary. (3) The flat-top noise level and break as well as the resonant peak frequencies are inversely proportional to the external radius  $r_j$ . (4) Computed rms and  $f$ -spectra exhibit an overall increase in the variability with energy. Comparison with observed variability features, especially in the hard-intermediate states of X-ray binaries, are discussed.

**Key words:** accretion, accretion discs – X-rays: binaries.

## 1 INTRODUCTION

X-ray binaries (XRBs) exhibit large variability on various time-scales. While their spectral states and their accretion rates are typically changing from weeks to days [see e.g. the different canonical states observed in black hole binaries (BHBs), as defined by McClintock & Remillard 2003; Homan & Belloni 2005; Belloni 2009 and references therein], their light curves exhibit drastic changes from hours to milliseconds. Several tools are now used in order to analyse these timing features (see e.g. van der Klis 2004 for a review), such as cross-correlation between different energy bands (which allows us to infer the so-called time lags), but the most commonly used is still the Fourier analysis via the computation of power spectral density (PSD).

Despite its known limitations (e.g. signal phase lost in the analysis), any attempt to model the physics of XRBs has to take into account the various features observed in the PSD and its evolution when the source transits from a state to another. In the so-called

hard state, the level of the variability is high and the PSD harbour a band limited noise (BLN) shape extending up to a break frequency  $\nu_b$ . Large peaks, the so-called quasi-periodic oscillations (QPOs), can also be observed. In the soft state, the Poissonian noise usually dominates on all the frequency ranges and either weak QPOs or none at all are detected. Different types of QPOs (called A, B and C) can be identified depending on the value of their frequency, their strength and even their time lags (see van der Klis 2004 or Casella et al. 2004 and references therein). However, if QPOs are remarkable features, the major part of the variability is usually aperiodic. As for energy spectra, variability evolves during time: in general, the overall variability decreases as the spectrum softens, with frequencies increasing, until in the soft state where the BLN reaches a low level (see e.g. Belloni et al. 2005; Belloni 2009).

Several models intending to interpret variability features focus on the QPO phenomena. For the high-frequency QPOs ( $\nu > 100$  Hz), lense-thirring precession (see e.g. Stella & Vietri 1998) or beating frequency between particular orbits (Lamb & Miller 2003) has been proposed. For the low-frequency QPOs (LFQPOs;  $0.01 < \nu < 100$  Hz), fewer models are available (see e.g. Tagger & Pellat 1999 or Titarchuk & Shaposhnikov 2005; see also Stella & Vietri 1998),

\*E-mail: cabanac@cesr.fr

but they usually try to explain the observed correlation between frequencies and/or other observables, without taking into account the whole emitting process. However, it is worth noting that it is in the highest energy bands that the X-ray flux is observed as being highly variable. In contrast, in most of the available models, the source of variability lies in the geometrically thin accretion disc, which emits mainly at lower energies. Note that some observations also suggest directly that the disc is less variable than the corona (see e.g. Churazov, Gilfanov & Revnivtsev 2001; Rodriguez, Corbel & Tomsick 2003; see also Wilkinson & Uttley 2009). In consequence, a proper model for the variability in BHB has to deal with the radiative transfer between the disc and the corona.

A few models have already been proposed in the literature. For instance, a full modelling of the BLN component has been attempted by Misra (2000) in the framework of a ‘transition disc model’: following the Nowak et al. (1999) idea, an acoustic wave is propagating within the accretion disc. In this framework, the author considers only the propagation to occur in one direction towards a central sink. This model is then used to explain qualitatively the general shape of the power spectra and lag energy dependencies observed in Cyg X-1.

Psaltis & Norman (2000) tried to model the filter effect of a narrow annulus in a geometrically thin disc. However, the nature of this annulus is not specified and its typical extension is  $\delta r/r < 10^{-2}$ . They also neglect the contribution of the radial pressure forces. In this framework and depending on the mode of oscillation chosen, the external perturbation is shown to be modulated in amplitude according to the exciting frequency. The square of the response in pressure exhibits Lorentzians which could account for the observed behaviour in black hole (BH) or neutron star (NS) binaries. In a similar spirit, Lee, Abramowicz & Kluźniak (2004) studied numerically the response to radial perturbations in an accretion torus. They showed that resonances could occur and become larger when the frequency differences between the radial and vertical epicyclic frequencies were half the forcing frequencies.

One of the very first attempts to evaluate the effect of propagation in a Comptonizing region on the timing behaviour was examined by Miyamoto et al. (1988). They showed that the tight period dependence of the observed time lags in Cyg X-1 could not be accounted for by the inverse Compton scattering process only. In another framework, Życki & Sobolewska (2005) tested their model of variability (Życki 2003), where the variable emission responsible for the noise component is attributed to multiple active regions/perturbations moving radially towards the central BH. The QPOs are obtained by modulating either the reflection amplitude, the heating rate, the covering factor of the reprocessor or the column density value. They predict for each of these cases the corresponding power and  $f$ -spectra (for a definition of  $f$ -spectra, see Revnivtsev, Gilfanov & Churazov 1999) and the time lag energy dependencies. In a subsequent paper, Sobolewska & Życki (2006) tested their model on real data and concluded that within this framework, the QPO spectra in the hard state are always softer than the normal average spectra and cold disc oscillations might then be responsible for the LFQPO. On the other hand, when the energy spectra get softer, the QPO spectra are harder and the LFQPO might then originate from the hot plasma.

In a more recent study, Schnittman, Homan & Miller (2006) try to model the oscillation of a torus in the Kerr metric, via three radiative processes: a thin emission line, then a thick one and finally an optically thick thermal emission process. They manage to reproduce some of the properties of C-type QPOs, especially the observed increase of the amplitude with the inclination of the system.

In this paper, we present a new approach that deals with the radiative transfer to an oscillating corona. These oscillations are assumed to be due to a magneto-acoustic wave propagating within the corona, modulating the efficiency of the Comptonization process on embedded soft photons. These basic ingredients give a promising framework to reproduce the main timing features of the XRB in hard and hard-intermediate states (HIMS), such as the BLN continuum and C-type LFQPO. The assumptions of the models and wave equation solutions are detailed in Section 2. An analytical study in the linear approximation is discussed in Section 3 and compared with Monte Carlo simulations in Section 4. We finally discuss the main results of this toy model and the comparison to observation in Section 5.

## 2 THE MODEL

### 2.1 Basic assumptions

The general structure of the model is sketched in Fig. 1. A hot optically thin cylindrical medium is assumed, hereafter called the ‘corona’. It is limited radially by its inner and outer radii  $r_i$  and  $r_j$ , respectively. This corona has thus a ring shape of typical height  $h_c$ . This geometry agrees with the observations that suggest the X-ray corona to be closely linked to the base of the jet in the XRB (e.g. Markoff, Falcke & Fender 2001; Fender, Belloni & Gallo 2004; Markoff, Nowak & Wilms 2005). Then the inner radius  $r_i$  can be identified as the last stable orbit close to the central compact object. On the other hand,  $r_j$  can be compared to the transition radius between an outer standard accretion disc and the inner hot corona, a geometry commonly invoked in the XRB (e.g. Esin, McClintock & Narayan 1997; Ferreira et al. 2006; Done, Gierliński & Kubota 2007).

In this paper, no hypothesis is done on the physical origin of these radii. For simplicity, the corona is assumed to have, at rest, a constant temperature  $T_0$  and density  $n_0$  and consequently a constant pressure  $P_0$ . We then consider that pressure instabilities at the external radius  $r_j$  generate a sound wave within this thermalized plasma. The origin and the nature of these instabilities are not discussed in this paper, since we focus only on the radiative response of the corona. We assume these instabilities to have a white noise spectrum (i.e. the same amplitude for all excitation frequencies) which corresponds to a Dirac perturbation in the temporal domain, i.e. we limit our study to the corona transfer function. For the sake of simplicity, we also restrict our calculation to the 1D case, i.e. the wave will only propagate radially at the sound velocity:

$$c_s = \sqrt{\frac{kT_0}{m_p}} \simeq 3.1 \times 10^8 \left( \frac{T_0}{100 \text{ keV}} \right)^{1/2} \text{ cm s}^{-1}. \quad (1)$$

In the last expression,  $T_0$  is in keV. It is important to note that there are simplifications which make this paper only a first step. Once additional complications such as incorporating the effects of rotation are introduced, they might lead to some revision of the scenario presented here. This will be addressed in a forthcoming paper. Note, however, that the nature of the corona and hence its exact rotation profile are still mainly unknown.

Finally, we suppose a blackbody seed photon field of temperature  $T_{\text{seed}}$  emitted isotropically at the corona mid-plane (i.e. at  $z = 0$ ; see Fig. 1). These seed photons will then be Comptonized in the corona producing a variable X-ray emission.

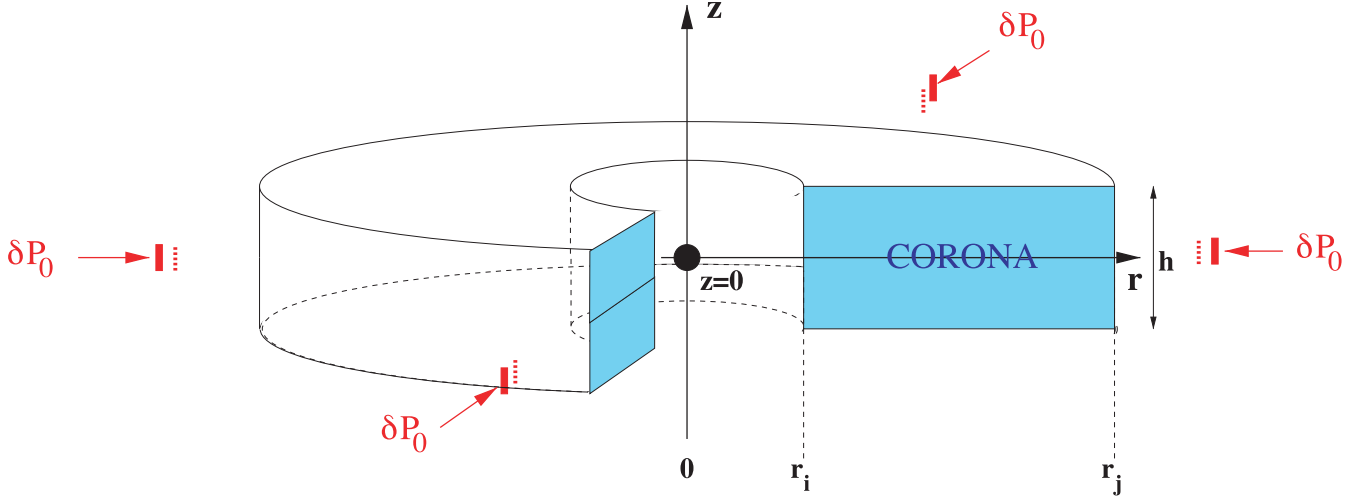


**Figure 1.** Sketch of the model geometry. The corona is assumed to harbour cylindrical symmetry. It extends from its inner radius  $r_i$  to its outer radius  $r_j$  and its height is  $h_c$ . Non-specified white noise excitations are assumed to occur at  $r_j$  then triggering (magneto) sonic waves in the corona. The resulting X-ray luminosity is then computed through thermal Comptonization of embedded soft photons.

## 2.2 Wave equation

In cylindrical 1D geometry, in the absence of local damping or excitation, and neglecting the rotation, the basic wave propagation equation can be written as

$$\frac{1}{r} \frac{\partial}{\partial r} \left( r \frac{\partial p}{\partial r} \right) - \frac{1}{c_s^2} \frac{\partial^2 p}{\partial t^2} = 0. \quad (2)$$

$p(r, t)$  is the perturbation in pressure given by, in complex notation and for a given frequency  $\nu = \omega/2\pi$ ,

$$p(r, t) = p_r(r) \exp^{i(-\omega t)}. \quad (3)$$

Introducing the new variable  $x = \frac{\omega}{c_s} r$  and putting equation (3) in equation (2), we get

$$x^2 \frac{d^2 p_r}{dx^2} + x \frac{dp_r}{dx} + x^2 p_r = 0. \quad (4)$$

The general solution to these equations is a linear combination of Hankel's functions of the zeroth order  $H_0^1$  and  $H_0^2$  (Abramowitz & Stegun 1964):

$$p(x, t) = [\alpha H_0^1(x) + \beta H_0^2(x)] e^{-i\omega t}, \quad (5)$$

$\alpha$  and  $\beta$  being determined by the boundary conditions. Note that the above solution is similar to the one obtained by Nowak et al. (1999) or Titarchuk & Shaposhnikov (2005), despite the fact that these authors used only  $H_0^1$  instead of a linear combination of  $H_0^1$  and  $H_0^2$  as a solution.

## 2.3 Boundary conditions: total reflection at the internal radius

At the external radius of the corona  $r_j$ , we assume a constant excitation  $p_0^1$  (white noise hypothesis):

$$p(x_j, t) = [\alpha H_0^1(x_j) + \beta H_0^2(x_j)] e^{-i\omega t} = p_0 e^{-i\omega t}, \quad (6)$$

where  $x_j = x(r = r_j)$ . The closure relationship will be given by the behaviour of the wave at the internal radius  $r_i$ . We will, as a primary assumption, consider that there is no transmission of the wave and

hence total reflection in  $r_i$ . If  $r_i$  is equal to or close to the last stable orbit, one would indeed expect the density of the corona to drop quickly inside this radius and hence the pressure as well. It thus gives

$$p(x_i, t) = [\alpha H_0^1(x_i) + \beta H_0^2(x_i)] e^{-i\omega t} = 0, \quad (7)$$

where  $x_i = x(r = r_i)$ . The system of equations (6) and (7) can be solved in order to obtain  $\alpha$  and  $\beta$ :

$$\alpha = p_0 \frac{H_0^2(x_i)}{H_0^2(x_i)H_0^1(x_j) - H_0^1(x_i)H_0^2(x_j)} \quad (8)$$

$$\beta = p_0 \frac{-H_0^1(x_i)}{H_0^2(x_i)H_0^1(x_j) - H_0^1(x_i)H_0^2(x_j)}. \quad (9)$$

## 3 ANALYTICAL SOLUTIONS IN THE LINEAR AND ZERO-PHASE APPROXIMATIONS

In this section, we infer the shape of the expected PSD in the simple case, where the radiative response of the corona depends linearly on the local perturbation. This appears to give analytical results in good agreement with our Monte Carlo simulations detailed in the next section.

The corona being optically thin, the luminosity  $dL_0$  emitted locally at rest in a ring of radius  $r$ , width  $dr$  and height  $h_c$  is proportional to its emissivity per unit volume  $\eta_0$ :

$$dL_0(r) = \eta_0 2\pi r dr h_c. \quad (10)$$

In the presence of the sonic wave, the luminosity  $dL(r, t)$  of this ring varies in time and we will make the assumption that its relative variation  $(dL - dL_0)/dL_0$  is a linear function of the relative pressure perturbation  $p(r, t)/P_0$ :

$$\frac{dL(r, t) - dL_0(r)}{dL_0(r)} = C_{\text{lin}} \frac{p(r, t)}{P_0}. \quad (11)$$

$C_{\text{lin}}$  is the constant of proportionality which is in complete generality a function of the perturbation frequency. However, if the delays implied by the multiple diffusions of the photon inside the corona are low compared to the period of the wave, a little phase delay

<sup>1</sup>Note the difference between  $p_0$ , the pressure perturbation imposed in  $r = r_j$  and  $P_0$  the corona pressure at rest.

is expected between the pressure wave and the luminosity. Hence,  $C_{\text{lin}}$  will be a real number independent of  $\omega$ . This is what we call the ‘zero-phase approximation’. It is usually verified in optically thin plasma where photons travel a few  $h_c$  before escaping (see e.g. Malzac & Jourdain 2000). Then a rough estimate of the time spent by the photons inside the corona compared to the period  $2\pi/\omega$  of the wave gives

$$\frac{\omega}{2\pi} \frac{h_c}{c} = \frac{1}{2\pi} \frac{h_c}{r} \frac{c_s}{c} x. \quad (12)$$

It is generally much smaller than 1 in the cases we are interested (i.e. corona aspect ratio  $h_c/r < 1$  and corona temperature of a few tens to hundreds of keV) unless  $x$  becomes of the order of 100 or 1000.

Combining equations (10) and (11), we obtain

$$dL(r, t) = \eta_0 \left( 1 + C_{\text{lin}} \frac{p(r, t)}{P_0} \right) 2\pi r dr h_c. \quad (13)$$

The previous equation integrated on the whole volume of the corona gives

$$L = L_0 + \underbrace{\eta_0 \frac{2\pi h_c C_{\text{lin}}}{P_0} \int_{r_i}^{r_j} p(r, t) r dr}_{\equiv L_{\sim}}, \quad (14)$$

$$\text{with } L_0 = \pi \eta_0 h_c (r_j^2 - r_i^2) = \pi \eta_0 h_c x_j^2 \frac{c_s^2}{\omega^2} (1 - \xi^2), \quad \text{and}$$

$$\xi \equiv \frac{r_i}{r_j} = \frac{x_i}{x_j}. \quad (15)$$

Note that relationship (14) is only valid if the emissivity per unit volume  $\eta_0$  of the corona, at rest, is uniform, which is a direct consequence of our assumptions of constant temperature and density  $T_0$  and  $n_0$ , respectively.

### 3.1 Power spectra obtained with large vertical wavelength and total reflection in $r_i$

Using equation (5), the expression of the perturbation in luminosity  $L_{\sim}$  becomes

$$L_{\sim} = \frac{2L_0 C_{\text{lin}}}{P_0} \frac{e^{-i\omega t}}{x_j^2 (1 - \xi^2)} \int_{\xi_j}^{x_j} [\alpha H_0^1(x) + \beta H_0^2(x)] x dx. \quad (16)$$

Hankel’s functions present in  $\alpha$  and  $\beta$  (see equations 8 and 9) are easily integrated (see Abramowitz & Stegun 1964) and hence the

previous equation leads to

$$L_{\sim} = \frac{2L_0 C_{\text{lin}} p_0}{P_0} \frac{e^{-i\omega t}}{x_j^2 (1 - \xi^2)} M_{x_j, \xi} \quad (17)$$

with

$$M_{x_j, \xi} = x_j \frac{H_{0,i}^2 (H_{1,j}^1 - \xi H_{1,i}^1) - H_{0,i}^1 (H_{1,j}^2 - \xi H_{1,i}^2)}{H_{0,i}^2 H_{0,j}^1 - H_{0,i}^1 H_{0,j}^2}. \quad (18)$$

$H_1^2$  and  $H_1^1$  are Hankel’s functions of the first order and the index  $i$  or  $j$  corresponds to the point where Hankel’s function is evaluated, i.e.  $x_i$  or  $x_j$  respectively. It is also easy to demonstrate that the function  $M$  is real in the case of total reflection (both the numerator and denominator are pure imaginaries and hence the ratio is real).

The PSD  $P_v \equiv |L_{\sim}|^2 / L_0^2$  can then be directly deduced from equation (17):

$$P_v \equiv |L_{\sim}|^2 / L_0^2 = \left| 2C_{\text{lin}} \frac{p_0}{P_0} \frac{M(x_j, \xi)}{x_j^2 (1 - \xi^2)} \right|^2. \quad (19)$$

It is directly proportional, due to our linear assumption, to the input perturbation through the term  $2C_{\text{lin}} p_0 / P_0$  but it is also modulated by the intrinsic response of the corona through the function  $M(x_j, \xi) / [x_j^2 (1 - \xi^2)]$ .

In the zero-phase approximation (see above)  $C_{\text{lin}}$  is real, and we can find asymptotic expressions of the PSD for low and high frequencies. For low frequencies, the function  $M$  can be approximated to (see Appendix A)

$$M(x_j, \xi) \underset{x_j \rightarrow 0}{\sim} x_j^2 \left( \frac{1}{2} - \frac{\xi^2 - 1}{4 \ln(\xi)} \right). \quad (20)$$

Hence, the PSD  $P_v$  (which is inversely proportional to  $x_j^2$ ) tends to a constant. At high frequencies, Hankel’s functions tend to cosine functions whose amplitudes are proportional to  $x_j^{-1/2}$  and thus  $P_v \propto x_j^{-2}$ .

Examples of PSD given by equation (19) are plotted in Fig. 2 as a function of the reduced frequency  $x_j = v/v_j$ , with  $v_j = 2\pi c_s / r_j$ . As expected, a flat-top noise component at low frequencies and a red noise at high frequencies are present. The break frequency scales like  $v_b \sim 2.5 v_j \propto c_s / r_j$  when  $\xi \rightarrow 0$  and  $v_b \sim \pi v_j / (1 - \xi)$  when  $\xi \rightarrow 1$  (see some examples plotted in the right-hand panel of Fig. 2). To determine this value of the break frequency, we fitted the analytical PSD obtained with a zero-centred Lorentzian, following the definition of Belloni, Psaltis & van der Klis (2002). The PSD also exhibits a peak around the break frequency and oscillations

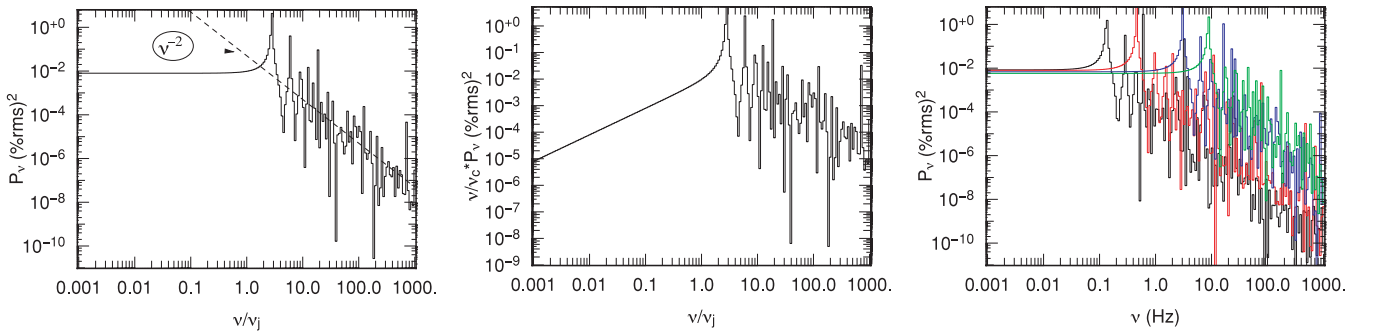


**Figure 2.** Left: power spectrum plotted in reduced frequency  $x_j = v/v_j$  (with  $v_j = 2\pi c_s / r_j$ ) for a single-zone corona with  $\xi = 10^{-2}$ ,  $C_{\text{lin}} = 1$  and  $\delta P_0 / P_0 = 0.1$ . Centre: same spectrum plotted in  $v/v_j$ . Right: PSD plotted in true frequency and its evolution when moving  $r_j$  inwards only. Here,  $M = 10 M_{\odot}$ ,  $r_i = 2 R_g = 3 \times 10^6$  cm and  $kT_0 = 100$  keV (hence  $c_s = 3.1 \times 10^8$  cm s $^{-1}$ ). Black:  $r_j = 680 R_g = 10^9$  cm, red:  $r_j = 200 R_g = 3 \times 10^8$  cm, blue:  $r_j = 68 R_g = 10^8$  cm, green:  $r_j = 14 R_g = 2 \times 10^7$  cm. [Note that (per cent rms) $^2$  (at  $v = 0$ ) slightly decreases and  $v_b$  increases when the external radius of the corona decreases, though the effect is tiny here.]

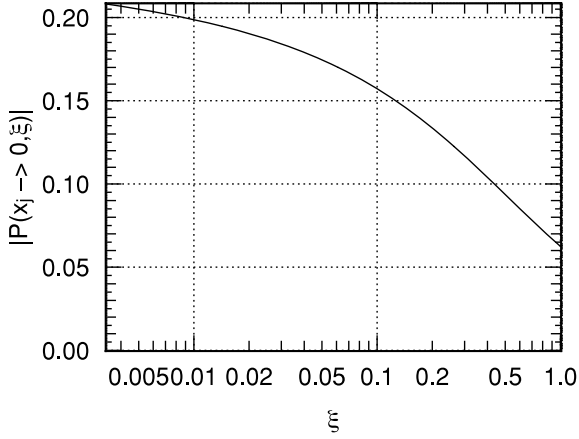


**Figure 3.** Dependency of the reduced PSD power at lowest frequencies ( $x_j \rightarrow 0$ )  $\frac{P_{x_j}(x_j \rightarrow 0)}{C_{lin} \frac{p_0}{p_0}}$  (see equation 19) as a function of the ratio  $\xi = r_i / r_j$ .

above it as expected from Hankel's function. The ratio of the frequencies of the first peak to the second one is predicted to be close to 2. Note therefore that the frequencies depend on the value of the outer radius of the inner region. We also noted that in our model, the QPO peaks around the break frequency.

Moreover, the PSD plateau, at low frequencies, slightly decreases when  $\xi$  increases. This is due to the behaviour of the modulation function  $M(x_j, \xi) / [x_j^2(1 - \xi^2)]$  at low frequency (i.e. when  $x_j$  tends to 0). It is plotted versus  $\xi$  for  $x_j = 0$  in Fig. 3 and shows a decrease from about 25 per cent for  $\xi = 0$  to about 5 per cent for  $\xi = 1$ .

### 3.2 Wave transmission in $r_i$

The oscillations present above the break frequency in the PSD (see Fig. 2) are due to the infinite resonances at the eigenfrequencies of the corona due to the assumption of total reflection in  $r_i$  and no wave damping. This total reflection hypothesis can be relaxed by assuming that part of the wave is transmitted in  $r_i$  in a medium of different sound velocity. An impedance adaptation then occurs between the two media, depending on the value of the acoustic impedance of the system  $Z = c_{s,2}/c_{s,1}$ , i.e. the ratio of the corona sound speed  $c_{s,1}$  to the sound speed  $c_{s,2}$  below  $r_i$ . The general form of the solution in the corona (medium 1) is similar to the one obtained before (equation 5) and hence can be written in reduced units  $x = \omega r / c_{s,1}$  as

$$p_1(x, t) = [\alpha H_0^1(x) + \beta H_0^2(x)] e^{-i\omega t}, \quad (21)$$

whereas, in medium 2, the transmitted wave is only progressive and hence has the following form:

$$p_2(x, t) = \zeta H_0^1\left(\frac{x}{Z}\right) e^{-i\omega t}. \quad (22)$$

In order to constrain  $\alpha$ ,  $\beta$  and  $\zeta$ , we need now three different equations. The first two equations come from the pressure continuity in  $r_i$  and  $r_j$ :

$$\alpha H_0^1(x_i) + \beta H_0^2(x_i) = \zeta H_0^1\left(\frac{x_i}{Z}\right) \quad (23)$$

$$\alpha H_0^1(x_j) + \beta H_0^2(x_j) = p_0. \quad (24)$$

The mass conservations in  $r_i$  give the third relation:

$$(\rho_1 S_1 v_1)_{r_i} = (\rho_2 S_2 v_2)_{r_i}, \quad (25)$$

with  $S_1 = 2\pi r_i h_1$  (respectively  $S_2 = 2\pi r_i h_2$ ) being the vertical surface in  $r_i$  in medium 1 (respectively medium 2) and  $v_1$  (respectively  $v_2$ ) the corresponding flow velocity. The link between  $v_m$  and the pressure perturbations  $p_m$  in each medium is obtained by applying the Euler equations ( $m = \{1, 2\}$ ):

$$\rho_m \frac{\partial v_m}{\partial t} = -\nabla p_m. \quad (26)$$

Hence, by using equations (21) and (22), we get

$$-i\omega \rho_1 v_1 = \frac{\omega}{c_{s,1}} [\alpha H_1^1(x) + \beta H_1^2(x)] \quad (27)$$

$$-i\omega \rho_2 v_2 = \frac{\omega}{Z c_{s,1}} \left[ \zeta H_1^1\left(\frac{x}{Z}\right) \right]. \quad (28)$$

Combining these two equations with equation (25) then gives

$$\frac{S_1}{c_{s,1}} [\alpha H_1^1(x_i) + \beta H_1^2(x_i)] = \frac{S_2}{Z c_{s,1}} \left[ \zeta H_1^1\left(\frac{x_i}{Z}\right) \right]. \quad (29)$$

We then need to constrain the corona height on both sides of  $r_i$ . We therefore assume that the corona is in hydrostatic equilibrium and in Keplerian motion. Consequently,  $h/r = c_s/v_{\text{Kepl}}(r)$  in each medium. As a result, at the internal radius  $r_i$ ,  $S_m/c_{s,m} = 2\pi r_i h_m/c_{s,m} = 2\pi r_i^2/v_{\text{Kepl}}(r_i)$ . This latter value is independent of the value of  $m$  and hence we obtain that  $S_1/c_{s,1} = S_2/c_{s,2} = S_2/(Z c_{s,1})$ . The mass conservation (equation 29) therefore reduces to

$$\alpha H_1^1(x_i) + \beta H_1^2(x_i) = \zeta H_1^1\left(\frac{x_i}{Z}\right). \quad (30)$$

The resolution of the previous system then gives the full solution in pressure within the corona:

$$p_1(x, t) = p_0 \frac{A H_0^1(x) + B H_0^2(x)}{A H_0^1(x_j) + B H_0^2(x_j)} e^{-i\omega t}, \quad (31)$$

with

$$A = H_1^2(\xi x_j) H_0^1\left(\frac{\xi x_j}{Z}\right) - H_0^2(\xi x_j) H_1^1\left(\frac{\xi x_j}{Z}\right) \quad (32)$$

$$B = H_1^1\left(\frac{\xi x_j}{Z}\right) H_0^1(\xi x_j) - H_0^1\left(\frac{\xi x_j}{Z}\right) H_1^1(\xi x_j). \quad (33)$$

In the linear approximation, we can obtain the outing PSD by following the same steps as in Section 3.1. The power spectrum from the main corona is therefore very similar to equation (19):

$$P_{x_j,1} = \left| 2C_{lin} \frac{p_0}{p_0} \frac{M_1(x_j, \xi)}{x_j^2(1 - \xi^2)} \right|^2, \quad (34)$$

with

$$M_1(x_j, \xi) = x_j \frac{C + D}{A H_0^1(x_j) + B H_0^2(x_j)}, \quad (35)$$

$$C = A [H_1^1(x_j) - \xi H_1^1(\xi x_j)], \quad (36)$$

$$D = B [H_1^2(x_j) - \xi H_1^2(\xi x_j)], \quad (37)$$

$A$  and  $B$  being given by equations (32) and (33), respectively.

Some examples of PSD are plotted in Fig. 4 for different values of the acoustic impedance  $Z = c_{s,2}/c_{s,1}$ . As expected, the resonances are cancelled when there is impedance adaptation (i.e.  $Z = 1$ ) between both media (see the left-hand panel of Fig. 4). The sound wave is in this case totally transmitted in  $r_i$ . Then the strength of the resonances is tuned by the impedance value as soon as it becomes different from unity and the higher the difference between both sound velocities, the stronger the resonances. Two PSD

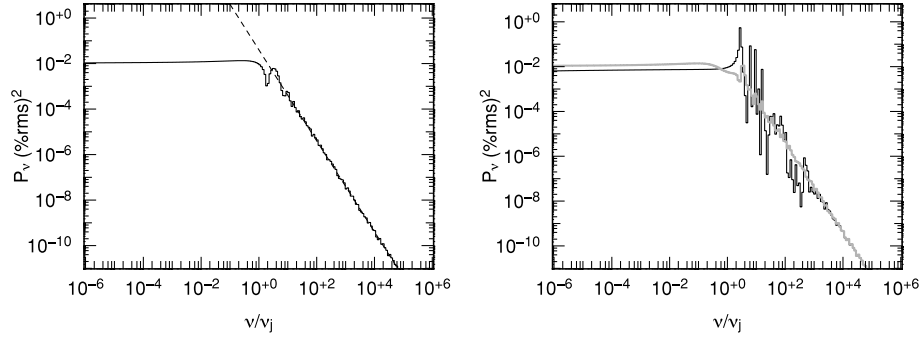


**Figure 4.** Left: power spectrum obtained for the corona when the sound velocities in media 1 and 2 are the same ( $Z = c_{s,2}/c_{s,1} = 1$ ). Right: PSD evolution when changing the value of the acoustic impedance. Thick grey curve:  $Z = 1.2$ , black:  $Z = 10$ .

examples with  $Z = 1.2$  and  $10$  are displayed in the right-hand panel of Fig. 4.

## 4 MONTE CARLO SIMULATIONS

### 4.1 A linear Comptonization code

In order to check the validity domain of the linear approximation that was used in the previous section, we performed Monte Carlo simulations of the radiative response of the corona. The Comptonization code used is linear, i.e. no feedback of the computed high-energy flux on the state of the corona is taken into account. The code uses the weighted Monte Carlo technique (see e.g. Pozdniakov, Sobol & Siuniae 1983). A monothermal blackbody distribution of temperature  $T_{\text{seed}}$  is assumed for the seed photons which are randomly drawn in the corona mid-plane ( $z = 0$ ). The temperature and optical depth of the corona at rest are fixed to  $T_0$  and  $\tau_0$ , respectively, implying a uniform pressure  $P_0$ . The wave propagation being supposed adiabatic, the perturbation in optical depth  $\delta\tau$  and temperature  $\delta T$  are given by

$$\frac{\delta T}{T_0} = \frac{\gamma - 1}{\gamma} \frac{p}{P_0}, \quad (38)$$

$$\frac{\delta\tau}{\tau_0} = \frac{1}{\gamma} \frac{p}{P_0}. \quad (39)$$

Then we impose sine perturbations in  $r = r_j$  with different frequencies but the same amplitudes  $\epsilon \equiv p_0/P_0$  (white noise). We assume that the total reflection at the internal radius and the pressure (and hence temperature and density) profile that the photon encounters while travelling within the corona is then given by equations (5), (8) and (9). For these simulations, both the linear and zero-phase approximation studied in the previous section were released. Hence, scattering after scattering, the photon will encounter during its travel some part of the corona where the perturbation in pressure is either positive or negative. The number of positive and negative zones in the corona is linked to the wavelength and hence the exciting frequency. The full Klein–Nishina cross-section is taken into account. The temporal evolution of the corona during the photon motion is also fully taken into account but appears to be negligible compared to the wave frequencies used, in agreement with our zero-phase approximation adopted in Section 3. We finally fit the corona X-ray emission with a sine function in order to obtain its amplitude  $L_{\sim}$  and potential phase delay. We repeat this procedure for different frequencies in order to build a power spectrum.

### 4.2 Results

Some examples of power spectra are plotted in Fig. 5 for different values of the external radius  $r_j$  and different energy bands indicated in the different panels. The other parameters are  $r_i = 3 \times 10^6$  cm,  $kT_0 = 100$  keV,  $\tau_0 = 1.4$  and  $kT_{\text{seed}} = 0.25$  keV. The amplitude of the modulation in pressure is set to an arbitrary value  $\epsilon = 0.15$ .

For such a low value of  $\epsilon$ , the PSD behaviour appears in good agreement with the linear hypothesis and zero-phase approximation studied in the previous section. Note that, thanks to the Monte Carlo simulations, we are also able to study the evolution of the power spectra with energy. Interestingly, the overall shape of the power spectra can also be mimicked by using sets of Lorentzians especially at high energy as shown in Fig. 5(f).

### 4.3 When does the linear approximation become invalid?

As shown in the previous section, for low values of the modulation amplitude  $\epsilon$ , the Compton emission of the corona agrees relatively well with the linear approximation. We expect, however, some deviation from linearity for larger modulation amplitudes, deviation that should also depend on the energy. This aspect is investigated here by increasing  $\epsilon$  in the simulations and then adjusting the corona spectral emission at different energy  $E$  with a quadratic polynomial, i.e.

$$\frac{L(\epsilon, t) - L_0}{L_0} \Big|_E \equiv \frac{\delta L(\epsilon, t)}{L_0} \Big|_E = [C_{\text{lin}}(E)\epsilon + C_{\text{quad}}(E)\epsilon^2] e^{-i\omega t}. \quad (40)$$

Hence, the energy-dependent parameters,  $C_{\text{lin}}$  versus  $C_{\text{quad}}$ , allow us to ‘quantify’ the linear and quadratic behaviour of the perturbation.<sup>2</sup>

Starting from a reference spectrum corresponding to  $kT_{\text{seed}} = 0.75$  keV,  $kT_0 = 75$  keV and  $\tau = 1.2$ , we simulate nine different spectra with values of  $\epsilon$  ranging from 0 to 60 per cent and fit the data with the polynomial given by equation (40) for different energy bins. The corresponding values of  $C_{\text{lin}}$  and  $C_{\text{quad}}$  are plotted in Fig. 6 as a function of the energy. They appear strongly energy dependent. Noticeably, they both cancel and change sign at a medium energy of about 2 keV, hint of a ‘pivot’ in the variable spectral emission of the corona.

This pivot is also clearly visible when comparing light curves at low and high energies such as those plotted in Fig. 7. Whereas

<sup>2</sup>Note that the parameter  $C_{\text{lin}}$  of equation (40) is not exactly the same as the one used in Section 3. It also includes all the geometry-dependent parts of the corona response (i.e. the term  $\frac{2M_{x_j, \xi}}{x_j^2(1-\xi^2)}$  present in equation 17).



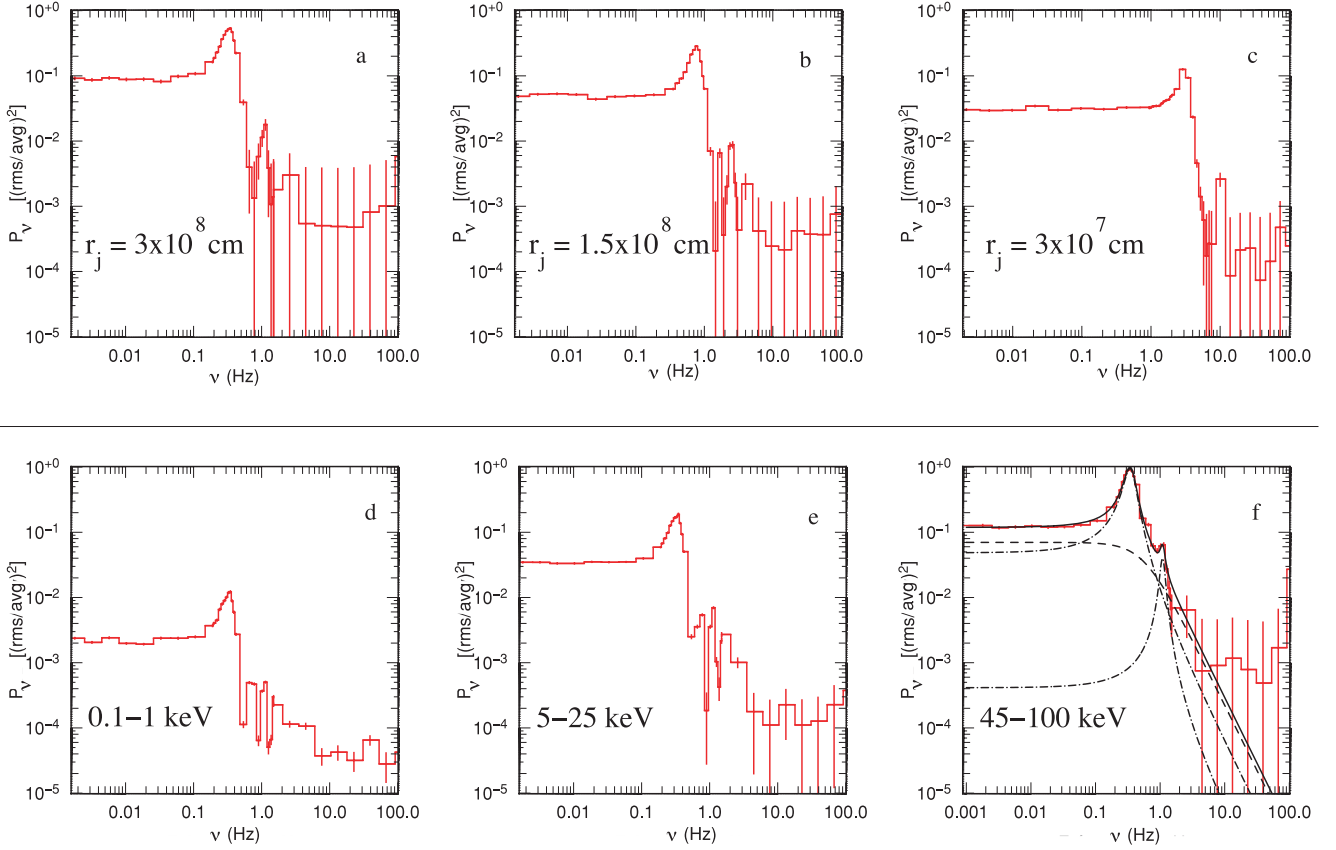


**Figure 5.** Evolution of the power spectrum obtained with either  $r_j$  or the energy band.  $1\sigma$  errors arising from the fit on the amplitude of the wave in flux are also plotted. See the text for the input parameter values. Upper panel (from left to right): PSD obtained for the 25–45 keV band. The QPO frequency moves upwards from 0.33 to 0.67 and 3.3 Hz when the external radius of the corona  $r_j$  moves inwards. Lower panel: evolution of the PSD with the energy band. The value of the external radius is  $r_j = 3 \times 10^8$  cm. Note the increase of the overall variability with the energy. In (f), the dashed curves are Lorentzians usually employed to fit the different components in PSDs of XRB.

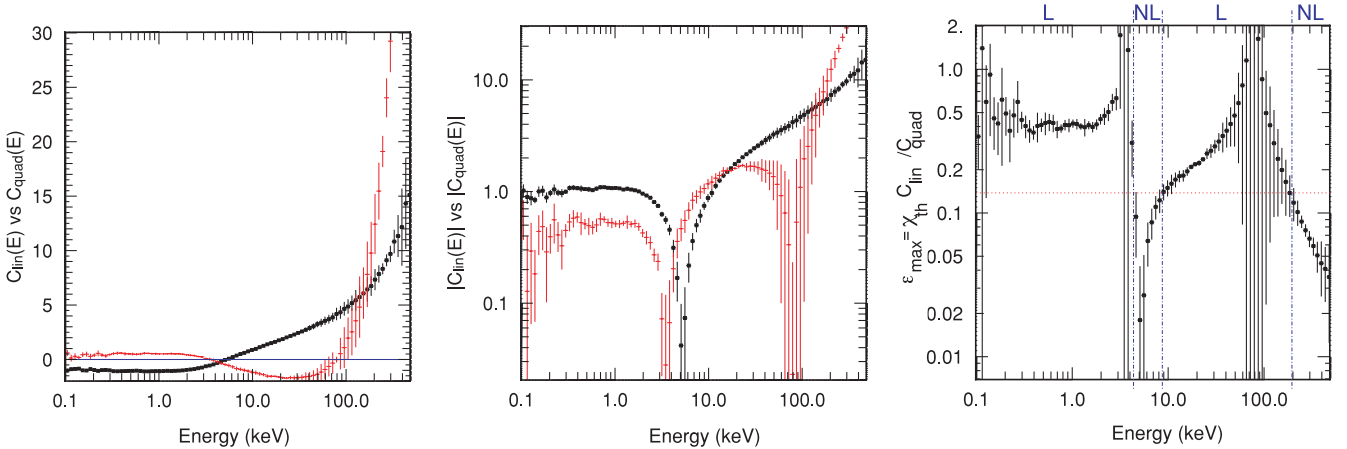


**Figure 6.** Left:  $C_{\text{lin}}$  (circle) versus  $C_{\text{quad}}$  (cross) value with linear coordinates on the y-axis (see the text for the parameter of the corona in the steady state). Under about 3 keV (the ‘pivot’), the value of  $C_{\text{lin}}$  is negative. This is a direct consequence of photon number conservation in the Compton scattering (see the text). Centre: the same as the right-hand plot, but in absolute value and the y-axis in log coordinates, to compare the magnitude. Above 10 keV,  $C_{\text{lin}}$  is higher than 1, emphasizing the effect of modulation in the flux by the perturbation in pressure. Right: plot of the  $\epsilon_{\text{max}}$  spectrum (see the text for explanation). Here,  $\chi_{\text{th}} = 0.2$ . If e.g.  $\epsilon = 0.15$  as plotted (dashed horizontal line), two linear and non-linear zones can be observed.

the high-energy light curve responds to the excitation coherently, the low-energy one (under the pivot) has a phase lag of  $\pi$ . This pivot is due to the Compton upscattering of low-energy photons which naturally produces a decrease in the number of soft photons

and, simultaneously, an increase in the number of the high-energy ones. Consequently, there is a  $\pi$  phase lag between the two energy domains. The quadratic term  $C_{\text{quad}}$  is cancelled a second time at higher energy ( $\sim 90$  keV in the simulation plotted in Fig. 6).



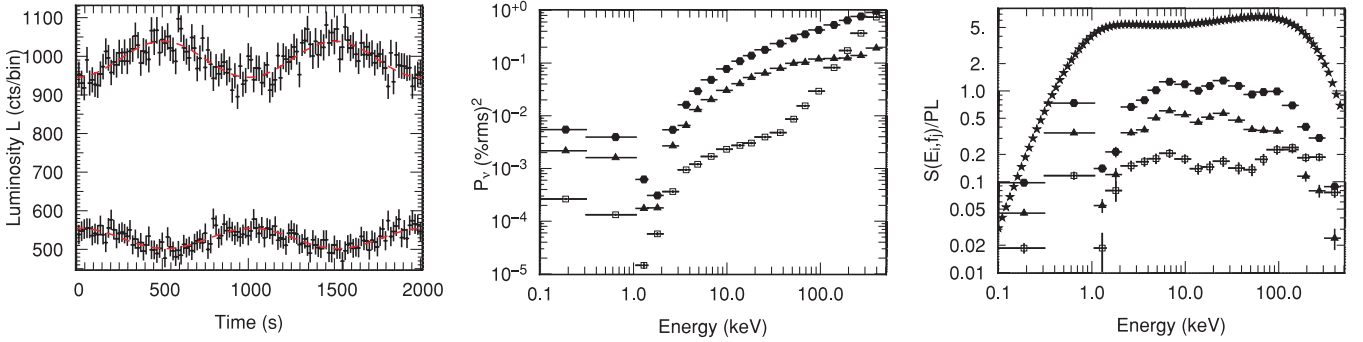


**Figure 7.** Left: light curves obtained for the lowest frequencies probed ( $\nu = 10^{-3}$  Hz), for two energy bands, and their best fit by a sine function (dashed curve). Upper plot: 0.25–1 keV. Lower plot: 2–3 keV. Note the phase lag of  $\pi$  between the high and low energies. Centre: ‘rms spectra’ for different frequency bands.  $\blacktriangle$ :  $10^{-3}$ – $10^{-1}$  Hz,  $\bullet$ :  $10^{-1}$ –0.7 Hz,  $\square$ : 0.7–1.5 Hz. Right: three lower curves: ratio of the  $f$ -spectra to a power-law model with photon index  $\alpha = 1.54$ , for different frequencies (the same symbol code as the centre panel). Upper curve ( $\star$ ): ratio of the time-averaged spectrum to a power law of index  $\Gamma_{\text{avg}} = 2.1$ . Time-averaged and 0.7–1.5 Hz spectra were rescaled for clarity.

By examining the trend at high energy in the centre panel of Fig. 6, it is worth noting that the value of  $C_{\text{lin}}$  is higher than 1 above 10 keV. This means that any fluctuation in pressure will produce an amplified radiative response of the corona at high energy. This is due to the pivoting of the spectrum, which acts as a ‘lever’ arm: the higher the energy bin, with respect to the pivot energy, the larger the luminosity variation.

To further investigate the domains of non-linearities, let us assume an arbitrary threshold  $\chi_{\text{th}}$  of the ratio of the quadratic to the linear terms in equation (40), i.e.  $\frac{C_{\text{quad}}\epsilon}{C_{\text{lin}}}$ , above which we estimate that the linearity hypothesis is no longer valid. This, in turn, determines different areas in the  $\epsilon/\chi_{\text{th}}$  versus energy plane (see Fig. 6) that agrees or disagrees with the linear approximation. For example, assuming a threshold  $\chi_{\text{th}}$  of 20 per cent means that we estimate that linearity is well satisfied as soon as  $\frac{C_{\text{quad}}\epsilon}{C_{\text{lin}}} < 0.2$ . For the set of parameters used in Section 4.2 and for which we obtain Fig. 6, this constrains the perturbation relative amplitude  $\epsilon$  to be smaller than  $\epsilon_{\text{max}} \simeq 50$  per cent =  $2.5\chi_{\text{th}}$  in the 0.1–3 keV energy band and smaller than  $\epsilon_{\text{max}} = 30$  per cent in the 10–40 keV band. For high values of  $\epsilon$ , say e.g.  $\epsilon = 0.7$ , the whole energy domain is non-linear. For lower values, say e.g.  $\epsilon = 0.15$  as plotted by the horizontal line in the right-hand panel of Fig. 6, two linear and two non-linear zones can be noted.

#### 4.4 Energy dependence of the variability

Finally, the strength of the variability and its evolution with energy is investigated. For this purpose, we computed and plotted in Fig. 7 the so-called rms spectra and  $f$ -spectra. These ‘variability spectra’ were computed for three spectral ranges: at the lowest frequencies, where the PSD is flat ( $10^{-3}$ – $10^{-1}$  Hz), near the resonance ( $10^{-1}$ –0.7 Hz) and after (0.7–1.5 Hz).

As expected from the behaviour of  $C_{\text{lin}}$ , the presence of the pivot leads to a drastic decrease of the rms at around 2 keV for all the frequencies studied, which is a strong prediction of the model, even if the position of this pivot in energy depends on several input parameters such as the seed photon temperature. After this, the variability increases without any cut-off at high energy. This is due to the fact that the wave in the corona also modulates the temperature of the high-energy electrons and hence the position of the cut-off in the high-energy spectrum. The higher the modulation, the larger the cut-off. An increase in the variability of the 0.7–1.5 Hz component is also predicted above  $\sim 100$  keV.

$f$ -spectra were also computed, following the definition of Revnivtsev et al. (1999) and adopting the same three frequency bands as above. Such spectra were then fitted between 2 and 150 keV by a power law. Their photon indices are decreasing with increasing frequencies as they are equal to  $1.61 \pm 0.02$  for the  $10^{-3}$ – $10^{-1}$  Hz band,  $1.53 \pm 0.01$  for the  $10^{-1}$ –0.7 Hz band and  $1.48 \pm 0.05$  for the 0.7–1.5 Hz band. In contrast, the time-averaged spectrum has a higher photon index ( $\Gamma_{\text{avg}} \sim 2.1$ ). The ratio of the obtained  $f$ -spectra to a power law of index 1.53 is plotted in Fig. 7, and also the ratio of the time-averaged spectrum to a power law of index 2.1. The time-averaged and the  $f$ -spectra exhibit a quite sensible deviation from the simple power-law model. This discrepancy with a power law is, however, more emphasized in the  $f$ -spectra than in the time-averaged spectra.

## 5 DISCUSSION

The timing response of an oscillating corona in cylindrical geometry is investigated, the corona acting as a filter when responding to a perturbation in pressure generated at its external radius. In the case of total reflection at the internal radius, infinite resonances may occur. They may be damped in the case of acoustic impedance adaptation between the corona and the external medium. We have shown that the filtering effect of the corona leads to power spectra with a broad-band shape well fitted by a Lorentzian centred in  $\nu = 0$  (see Fig. 5). Moreover, the resonances produce a major peak at the PSD break and smaller peaks at higher frequency. The characteristic frequencies of the PSD break and peaks scale with  $\nu_j = 2\pi c_s/r_j$ . For a  $10 M_{\odot}$  BH, an outer corona radius  $r_j = 200 R_g$  and a corona temperature  $kT_0 = 100$  keV (i.e. a sonic velocity  $c_s = 3.1 \times 10^8$  cm s $^{-1}$ ), this gives  $\nu_j = 0.17$  Hz. These power spectra are thus relatively similar to the one observed in the HIMS of X-ray transients, whose shapes are well fitted by three to four Lorentzians peaking at different frequencies from tens of hertz (for the break and the LFQPO) to hundreds of hertz (for the high-frequency QPO, see e.g. Nowak 2000 or Pottschmidt et al. 2003).

Interestingly, our low-frequency peak is always of the order of the frequency break  $\nu_b$  (both scaling with  $\nu_j$ ). This is also in agreement with the observed correlations between  $\nu_b$  and the LFQPO  $\nu_{\text{LFQPO}}$  (Wijnands & van der Klis 1999; Belloni et al. 2002; Klein-Wolt & van der Klis 2008). We note, however, that  $\nu_{\text{LFQPO}}$  is usually five times higher than  $\nu_b$ , especially in the Wijnands & van der Klis (1999) relationship. We note, however, that in the equivalent

correlation plotted in fig. 11 of Belloni et al. (2002), the lower branch shows a correlation between the break frequency  $\nu_b$  and the typical frequency of the ‘hump’ ( $\nu_h$ ), with a ratio close to 1. Finally, the ratio between the first two peak frequencies is close to 2 in our model, as is observed for several C-type QPOs.

Our model also predicts a decreasing PSD power and an increasing resonance peak frequency when decreasing the outer corona radius  $r_j$ . This is here again consistent with the general trend observed in the BHB where the PSD power decreases when the observed frequencies increase (BH anticorrelation; Belloni & Hasinger 1990). However in our model, this effect is low and could hence only account for a fraction of the observed anticorrelation. Indeed, the BH anticorrelation translates the fact that in  $\nu P_\nu$ , the different observed Lorentzians are peaking at roughly the same level, or equivalently that the rms-integrated variability remains roughly constant. An extra condition on the exciting process is therefore required, with an rms level that must decrease when the size of the corona decreases as well. The necessary condition would hence be that  $\delta P \propto r_j^\alpha$ , with  $\alpha \geq 0.5$ .

As shown in Fig. 7, we expect a  $\pi$  phase lag between the very low-energy and the high-energy light curves, which is a strong prediction of the model. This is a direct consequence of the assumed geometry, especially of the fact that the source of seed soft photons is assumed at the corona mid-plane. This source is necessarily on the line of sight of the observer. Then due to the photon number conservation during the Compton scattering process, the disappearance of the soft photons is directly compensated by an increase of the hard ones. Moreover, it depends on the pivot energy which crucially depends on the input parameters (especially  $kT_c$  and  $kT_{\text{soft}}$ ). In a geometry where the soft seed photons are produced outside the corona, this constraint can be easily relaxed. This would be the case of a soft photon field produced by an outer accretion disc. Such a geometry (inner hot corona surrounded by an outer accretion disc) is indeed generally believed to qualitatively well reproduce the inner region of the accretion flow around compact objects (i.e. Esin et al. 1997; Done et al. 2007). Note that with such geometry, a decrease in the outer corona radius  $r_j$  (which corresponds to the inner accretion disc) would imply an increase in the seed photons’ temperature and flux i.e. an increase in the corona coolings. Consequently, a softening of the X-ray spectrum should happen. Since a decrease in  $r_j$  also implies, in our model, an increase in the resonance peak frequencies, a correlation between the X-ray photon index and the QPO frequencies is expected. Such a correlation is indeed observed in different XRBs (Titarchuk & Shaposhnikov 2005).

The position of the pivot can also be drastically changed and moved towards lower energies if the seed photons’ typical energy is far lower than that considered here. For example, as suggested e.g. in Malzac & Belmont (2009), the soft photon contribution could originate from the synchrotron emission in optical and ultraviolet from the hot plasma.

We also demonstrated that  $C_{\text{lin}}$  increases after the pivot, whereas  $C_{\text{quad}}$  decreases again around 20 keV. The general increase of  $\delta L/L$  with the energy after the pivot (visible e.g. in the rms spectra plotted in Fig. 7) could be responsible in part for the observed increase of the variability with energy for the QPO and the continuum (for XTE J1550–564, see e.g. Cui et al. 1999). Alternatively, the observed decrease in the QPO harmonic strength in fig. 5 of Cui et al. (1999) could also be well explained by the drop in the value of  $C_{\text{quad}}$  after 30 keV. We can also note the similarity between the rms spectra plotted in fig. 5 of Cui et al. (1999), when the source is in its HIMS, and the one we obtained with our model. The increase of the QPO

and continuum variability between 2 and 20 keV is then a direct consequence of the Comptonization process.

We also observe a decrease in the power-law slope in the  $f$ -spectra when the frequencies get higher. This is consistent with the results obtained for Cyg X-1 in Revnivtsev et al. (1999). It is worth noting that these authors explained the presence of ‘wiggles’ in the  $f$ -spectra as a consequence of reflection features on an optically thick material. Our Monte Carlo simulations show, however, that these features can be generated by the Comptonization process only.

The non-linear domain is then investigated as a function of the energy. We demonstrated that if a reasonable arbitrary value of the non-linear to linear ratio is chosen, it is expected that the non-linear effects of the radiative response will occur only at very high and medium energies.

The choice of a cylindrical geometry has also an impact on the degree of loss of the input signal due to scatterings. The following arguments are similar to those discussed in previous studies, such as in e.g. Miller (1995). Indeed, unless one global oscillation takes place in the corona (which is the case at very low exciting frequencies), a photon may encounter alternatively positive and negative perturbations in pressure if it travels in the radial direction. It would consequently kill the effect of the input signal on the output light curve. We even expect this effect to be emphasized when looking at high energies, as, regardless of the optical depth of the medium chosen, a high-energy photon encountered a large number of scatterings. On the contrary, the oscillation will not be smeared out if the travel of the photon remains local.

As we chose a cylindrical geometry, the optical depth  $\tau \sim 1$  is relative to the vertical direction and hence this implies that in the azimuthal and radial directions  $\tau_{r,\theta} \gg 1$ . As a consequence, this is forcing the locality, relative to the radial wavelength of the perturbation, which in turn preserves the signal, whatever the output photon energy. As one goes towards a more spherical geometry, where  $\tau$  now becomes a measure of the radial optical depth,  $\tau$  in various directions becomes much less anisotropic. Looking at higher energies means looking at a larger range of sampled locations and hence smearing of the imparted variability signal for sufficiently small wavelengths of the perturbation.

While this simple model already provides very interesting timing behaviour and appears very promising to explain the main features observed in the PSD of XRB, significant improvements are needed to include different, and potentially important, physical effects.

For instance, we have shown that the effect of transmitting the wave in an inner medium results in softening the resonances and the gaps in the power spectra. But the kinematics of the corona could also play an important role. Assuming the corona located in the inner region of an accretion flow, some (differential) rotation is expected and we might expect the emitted frequency by each part of the corona to be Doppler shifted, smoothing the PSD in the same way emission lines can be smoothed in energy spectra. In the close vicinity of the central engine, the general relativistic effects should also significantly contribute to blur the PSD. The use of a non-uniform sound velocity profile (due to e.g. non-uniform corona temperature) along the radial or vertical direction is also expected to have some impact in this respect. But more importantly, including all these effects will result in a very different dispersion equation followed by the acoustic waves and thus in a significantly different behaviour of the radiative response of the corona.

We also used a single sound wave, but other acoustic waves could be present. For example, in the case of magnetic plasma Alfvén and both slow and fast magnetosonic waves, with velocities  $v_A$ ,  $c^-$  and  $c^+$ , should be used. The former do not generate density or pressure

perturbation. They are not expected to change the Comptonization efficiency, contrary to the magnetosonic ones. In the case of plasma in equipartition,  $c_s^2 = v_A^2$ , hence  $c^- = 0.54c_s$  and  $c^+ = 1.31c_s$ , and we do not expect significant changes compared to the sound wave case studied here.<sup>3</sup> However, for a plasma far from equipartition,  $c^- \sim c_s \neq c^+ \sim v_A$ . Therefore if both waves propagate in the medium, each component would be responsible for its own BLN and resonances in the power spectra. Multiple perturbing waves may then explain the multiple Lorentzian components generally needed to fit the PSD of XRB in hard states (e.g. Nowak 2000; Pottschmidt et al. 2003). Note however that in the HIMS, only two Lorentzians are necessary. If we identify in our framework the low-frequency Lorentzian ( $L_b$ ; see Belloni et al. 2002 for the labels of the different PSD components) with the propagation of a slow magneto-sonic wave and the lower upper frequency ( $L_1$ ) with the fast one, it would require a very high magnetization parameter for the plasma. Indeed, the observations give roughly  $v_1 \sim 50v_b$  (see e.g. tables 2 and 3 in Belloni et al. 2002), and since  $c^- \sim c_s$  and  $c^+ \sim v_A$ , it would imply that  $v_A^2/c_s^2 \sim 2500$ .

We also did not investigate the implied time lags generated by the Comptonization process. It is however known that such lags can be reproduced by pivoting in the spectra (see e.g. Poutanen & Fabian 1999 or K rding & Falcke 2004), and our models predict the presence of such a pivot.

More fundamentally, as we probe the timing response of the corona, it can be used as a complement to other variability models, as the shape of the input excitation is supposed here to be a white noise. The rms flux scaling found in both the active galactic nucleus and XRB (see e.g. Uttley & McHardy 2001) has demonstrated that the processes at the origin of the variability are, by essence, non-linear (Uttley, McHardy & Vaughan 2005). This is not necessarily in contradiction to our study since we only investigate what is the timing response of the corona, without taking into account the feedback process of the corona on the disc itself. Our model just examines the subsequent effects of the corona and in particular how the radiative transfer and the geometry of this optically thin medium could filter any input variability.

The present model does not intend to reproduce all the observed features concerning the XRB variability, especially due to its simplicity. The results obtained in this paper are however very promising for further investigations, and a more detailed analysis, including the effect of the corona rotation and geometry, will be presented in a forthcoming paper.

## ACKNOWLEDGMENTS

CC thanks J. Rodriguez, D. Hannikainen, D. Barret, A. Goldwurm, J.-M. Hameury, C. Done, P. Uttley, I. Papadakis and R. Belmont for useful discussions on the subject. The authors also thank the anonymous referee for his useful comments on the paper. This work has been supported by the French National Agency (ANR) through the project ‘Astro2flots’ ANR-05-JCJC-0020. TMB acknowledges support from contract PRIN INAF 2008.

## REFERENCES

Abramowitz M., Stegun I. A., 1964, Handbook of Mathematical Functions, 9th edn. Dover Press, New York

- Belloni T., ed., 2009, Lecture Notes in Physics Vol. 794, The Jet Paradigm – From Microquasars to Quasars. Springer-Verlag, Berlin/Heidelberg, p. 53
- Belloni T., Hasinger G., 1990, A&A, 227, L33
- Belloni T., Psaltis D., van der Klis M., 2002, ApJ, 572, 392
- Belloni T., Homan J., Casella P., van der Klis M., Nespoli E., Lewin W. H. G., Miller J. M., M ndez M., 2005, A&A, 440, 207
- Casella P., Belloni T., Homan J., Stella L., 2004, A&A, 426, 587
- Churazov E., Gilfanov M., Revnivtsev M., 2001, MNRAS, 321, 759
- Cui W., Zhang S. N., Chen W., Morgan E. H., 1999, ApJ, 512, L43
- Done C., Gierliński M., Kubota A., 2007, A&AR, 15, 1
- Esin A. A., McClintock J. E., Narayan R., 1997, ApJ, 489, 865
- Fender R. P., Belloni T. M., Gallo E., 2004, MNRAS, 355, 1105
- Ferreira J., Petrucci P.-O., Henri G., Saug  L., Pelletier G., 2006, A&A, 447, 813
- Homan J., Belloni T., 2005, Ap&SS, 300, 107
- Klein-Wolt M., van der Klis M., 2008, ApJ, 675, 1407
- K rding E., Falcke H., 2004, A&A, 414, 795
- Lamb F. K., Miller M. C., 2003, preprint (astro-ph/0308179)
- Lee W. H., Abramowicz M. A., Kluźniak W., 2004, ApJ, 603, L93
- McClintock J. E., Remillard R. A., 2003, in Lewin W., van der Klis M., eds, Cambridge Astrophys. Ser. Vol. 39, Compact Stellar X-ray Sources. Cambridge Univ. Press, Cambridge, p. 157
- Malzac J., Jourdain E., 2000, A&A, 359, 843
- Malzac J., Belmont R., 2009, MNRAS, 392, 570
- Markoff S., Falcke H., Fender R., 2001, A&A, 372, L25
- Markoff S., Nowak M. A., Wilms J., 2005, ApJ, 635, 1203
- Miller M. C., 1995, ApJ, 441, 770
- Misra R., 2000, ApJ, 529, L95
- Miyamoto S., Kitamoto S., Mitsuda K., Dotani T., 1988, Nat, 336, 450
- Nowak M. A., 2000, MNRAS, 318, 361
- Nowak M. A., Wilms J., Vaughan B. A., Dove J. B., Begelman M. C., 1999, ApJ, 515, 726
- Pottschmidt K. et al., 2003, A&A, 407, 1039
- Poutanen J., Fabian A. C., 1999, MNRAS, 306, L31
- Pozdniakov L. A., Sobol I. M., Siuniae R. A., 1983, Astrophys. Space Phys. Rev., 2, 189
- Psaltis D., Norman C., 2000, preprint (astro-ph/0001391)
- Revnivtsev M., Gilfanov M., Churazov E., 1999, A&A, 347, L23
- Rodr guez J., Corbel S., Tomsick J. A., 2003, ApJ, 595, 1032
- Schnittman J. D., Homan J., Miller J. M., 2006, ApJ, 642, 420
- Sobolewska M. A., Życki P. T., 2006, MNRAS, 370, 405
- Stella L., Vietri M., 1998, ApJ, 492, L59
- Tagger M., Pellat R., 1999, A&A, 349, 1003
- Titarchuk L., Shaposhnikov N., 2005, ApJ, 626, 298
- Uttley P., McHardy I. M., 2001, MNRAS, 323, L26
- Uttley P., McHardy I. M., Vaughan S., 2005, MNRAS, 359, 345
- van der Klis M., 2004, in Lewin W., van der Klis M., eds, Cambridge Astrophys. Ser. Vol. 39, Compact Stellar X-ray Sources. Cambridge Univ. Press, Cambridge, p. 39
- Wijnands R., van der Klis M., 1999, ApJ, 514, 939
- Wilkinson T., Uttley P., 2009, MNRAS, 397, 666
- Życki P. T., 2003, MNRAS, 340, 639
- Życki P. T., Sobolewska M. A., 2005, MNRAS, 364, 891

## APPENDIX A: LOW-FREQUENCY DEPENDENCE OF THE MODULATING FUNCTION M

Hankel’s functions can be expressed as a function of Bessel’s:

$$H_n^1(x) = J_0(x) - iY_0(x) \quad (A1)$$

$$H_n^2(x) = J_0(x) + iY_0(x). \quad (A2)$$

For low values of  $x$ , the equivalents of Bessel’s function are as follows:

$$J_0(x) \sim 1 \quad (A3)$$

<sup>3</sup>The above calculations were done with  $v_{A, \text{poloidal}} = 1/\sqrt{2}v_A$ .

$$Y_0(x) \sim \frac{2}{\pi} \left[ \ln \left( \frac{x}{2} \right) + \gamma \right] J_0(x) \quad (\text{A4})$$

$$J_1(x) \sim \frac{x}{2} \quad (\text{A5})$$

$$Y_1(x) \sim -\frac{2}{\pi x} + \frac{x}{\pi} \ln \left( \frac{x}{2} \right) - \frac{x}{2\pi} (-2\gamma + 1) \quad (\text{A6})$$

(Abramowitz & Stegun 1964), where  $\gamma$  is the Euler–Mascheroni constant. If Hankel’s functions are expressed in terms of Bessel’s functions, both the numerator and denominator of the function  $M$  (equation 18) are pure imaginary and the modulating function  $M$  writes as

$$M(x_j, \xi) = x_j \frac{J_{0,i}(Y_{1,j} - \xi Y_{1,i}) - Y_{0,i}(J_{1,j} - \xi J_{1,i})}{J_{0,i}Y_{0,j} - Y_{0,i}J_{0,j}} \quad (\text{A7})$$

$$= x_j \frac{N}{D}. \quad (\text{A8})$$

Using the four equivalents (A3)–(A6), the numerator  $N$  and denominator  $D$  write as

$$\begin{aligned} N = & \frac{-2}{\pi x_j} + \frac{2\xi}{\pi \xi x_j} + \frac{x_j}{\pi} \ln \left( \frac{x_j}{2} \right) - \frac{\xi^2 x_j}{\pi} \ln \left( \frac{\xi x_j}{2} \right) \\ & - \frac{x_j}{2\pi} (-2\gamma + 1) + \frac{\xi^2 x_j}{2\pi} (-2\gamma + 1) \\ & - \frac{2}{\pi} \left[ \ln \left( \frac{\xi x_j}{2} \right) + \gamma \right] \left( \frac{x_j}{2} - \frac{\xi^2 x_j}{2} \right) \end{aligned} \quad (\text{A9})$$

$$D = \frac{2}{\pi} \left[ \ln \left( \frac{x_j}{2} \right) \right] - \frac{2}{\pi} \left[ \ln \left( \frac{\xi x_j}{2} \right) \right]. \quad (\text{A10})$$

These equations can be rewritten as

$$\begin{aligned} N = & \frac{x_j}{\pi} \left[ \ln \left( \frac{x_j}{2} \right) - \xi^2 \ln \left( \frac{\xi x_j}{2} \right) \right. \\ & \left. - (1 - \xi^2) \frac{-2\gamma + 1}{2} - \ln \left( \frac{\xi x_j}{2} \right) - \gamma \right. \\ & \left. + \xi^2 \ln \left( \frac{\xi x_j}{2} \right) + \gamma \xi^2 \right] \end{aligned} \quad (\text{A11})$$

$$D = -\frac{2}{\pi} \ln(\xi). \quad (\text{A12})$$

Finally, we get

$$N = \frac{x_j}{\pi} \left[ -\frac{1 - \xi^2}{2} - \ln(\xi) \right] \quad (\text{A13})$$

$$D = -\frac{2}{\pi} \ln(\xi). \quad (\text{A14})$$

These last equations combined with equation (A8) lead to the result written in equation (20).

This paper has been typeset from a  $\text{\TeX}/\text{\LaTeX}$  file prepared by the author.